

# Multi-lepton signatures for scalar dark matter searches in coannihilation scenario

Sreemanti Chakraborti<sup>1,\*</sup> and Rashidul Islam<sup>1,†</sup>

<sup>1</sup>Indian Institute of Technology Guwahati, Guwahati 781 039, India

We revisit the scalar singlet dark matter (DM) scenario with a pair of dark lepton partners which form a vector-like Dirac fermionic doublet. The extra doublet couples with the SM leptonic doublet and the scalar singlet via a non-SM-like Yukawa structure. As a result, (1) since the extra fermionic states interact with other dark sector particles as well as the SM via gauge and Yukawa interactions, it gives rise to new DM annihilation processes including pair annihilation as well as coannihilation channels, and (2) such a Yukawa structure opens up new production channels for leptonic final states giving much enhancement in cross sections to search for dark matter in the LHC. Using suitable kinematic observables, we train a Boosted Decision Tree (BDT) classifier to separate enhanced but still feeble light leptonic signal from the backgrounds in an effective manner. On the other hand, same technique is applied to study  $\tau$ -tagged jets in search for DM signals.

## I. INTRODUCTION

Cosmological considerations and astrophysical observations have established beyond any reasonable doubt, the existence of the dark matter (DM). The satellite-borne experiments such as WMAP [1] and PLANCK [2] measured extremely precisely the cosmological relic abundance and it is given by  $\Omega_{\text{DM}} h^2 = 0.1199 \pm 0.0027$ ,  $h$  being the reduced Hubble constant. Though DM constitutes about 27% of the energy budget of the Universe, the particle nature of it remains an enigma. The search for a suitable candidate for particle dark matter is a longstanding problem [3–5]. The so-called Weakly Interacting Massive Particle (WIMP) is the most widely explored sector to resolve the discrepancy. Within the WIMP paradigm, the scalar singlet dark matter or scalar “Higgs-portal” scenario is perhaps the most studied of all the relevant scenarios of dark matter to explain the relic density [6–8]. Consequently, it went through immense scrutiny theoretically as well as experimentally (see for example Refs. [9, 10] for recent reviews of the current status of the Higgs portal scenario). We now know that the direct detection (DD) [11–14], indirect detection (ID) [15–17] and invisible Higgs decay [18–20] searches put a strong bound on the coupling of the Standard Model (SM) Higgs boson,  $h$  with the said scalar singlet, say  $S$ . Let us call this coupling  $\lambda_{hS}$ . These experiments constrain  $\lambda_{hS}$  to be very small. As a result, it gives an overabundance of relic density except around a small window around the resonance region,  $m_S \sim m_h/2$ .

However, one can improve the situation with scalar singlet DM using various alternatives, such as considering other symmetries within the dark sector [21–23] or adding new particles in the particle spectrum so as to arrange other portals [24–26] for DM annihilation without worsening the existing constraints. An interesting possibility in this context, called the *coannihilation* [27], is a widely studied feature in DM dynamics where the DM annihilates with another dark sector particle and the chemical equilibrium between the annihilating particles ensures the substantial depletion of DM number density. This feature is a very useful handle to revive the scenarios where direct detection bounds push relic density to overabundance. In such scenarios, coannihilation works efficiently as a DM number changing process without affecting the direct search measurements because the couplings involved in coannihilation are insensitive to direct detection channels.

In the present work, we will revisit the scenario of the scalar singlet dark matter with a pair of accompanying dark leptons which form a vector-like Dirac fermionic doublet. This dark sector doublet couples with the SM leptonic doublet and the scalar singlet via a novel Yukawa interaction which is less explored in the literature. There are two distinct interesting features of this model: (1) Since the new dark sector fermions form a doublet they will interact with the SM via gauge interaction as well as the new Yukawa coupling, which in turn will give rise to new annihilation channels, and (2) Such a Yukawa structure will open up new production channels for leptonic final states giving much enhancement in cross-sections to search for dark matter in collider environments like LHC through the said channel. Depending on the choice of parameters, here the DM annihilation can have three distinguishable stages, namely pair annihilation, coannihilation, and mediator annihilation. Here, it is to be noted that coannihilation scenarios in WIMP are mostly studied in the literature in the context of SUSY [28–30] and coloured coannihilating particles [31–33]. Our model discusses a leptophilic context and the coannihilation channels play an important role here due to the gauge interaction in the dark sector in addition to

\*Electronic address: [sreemanti@iitg.ac.in](mailto:sreemanti@iitg.ac.in)

†Electronic address: [rislam@iitg.ac.in](mailto:rislam@iitg.ac.in)

the new Yukawa coupling. This feature is significantly different from the cases explored in literature where the leptophilic Yukawa structure involves singlet dark sector partners with the DM candidate [34, 35].

As mentioned above, since the coannihilating partner<sup>1</sup> couples to the SM with gauge as well as Yukawa coupling, the leptonic search channels get a boost in cross-section from it and it is only logical to probe the said channel for collider signatures. Moreover, the leptonic channel gives cleaner signals than the other channels. Still, the collider searches of dark matter is a very challenging prospect. Note that any lepto-philic DM model like ours contributes to the calculation of muon  $g - 2$ . Very good agreement between the theoretical calculation and experimental measurements of muon  $g - 2$ ,  $\Delta a_\mu = a_\mu^{\text{Exp}} - a_\mu^{\text{SM}} = 268(63)(43) \times 10^{-11}$  [36] put a strong constraint on the new Yukawa couplings of the light SM leptons. However, there is no such bound for the production of  $\tau$ -leptons. Hence, it would be a good prospect to probe that channel for dark matter signatures in colliders. Our case is similar to the supersymmetric (SUSY) theories where stau is the coannihilating partner [28, 37–43].

Despite the leptonic channel getting a boost, the cross-section can still be smaller. So to probe light leptonic channels effectively, one must follow sophisticated techniques to separate signals from the backgrounds. The multivariate analysis is one such prospect. We perform Boosted Decision Tree (BDT) response to separate feeble light leptonic signal from the backgrounds in an effective manner. On the other hand, despite further enhancement in cross-section, the  $\tau$ -leptons mostly decay into hadronic jets resulting in difficulty in their reconstruction. We used  $\tau$ -tagged jets from the detector simulation with 60%  $\tau$ -tagging efficiency to perform the BDT response.

We organized the paper as follows. In Section II, we describe the contents of our model. The dark matter phenomenology, its formalism, and the observations from the relic density, direct and indirect detection calculation are discussed in Section III. Section IV contains the study of collider signatures at the LHC through multivariate analysis of light di-lepton as well as di- $\tau$ -lepton channel. Finally, we conclude our results in Section V.

## II. MODEL DESCRIPTION

As we described briefly in the Introduction, we want a model where the dark sector will consist of one or more coannihilating partners in addition to the scalar singlet dark matter. So, we consider a vector-like Dirac fermionic doublet,  $\Psi^T = (\psi^0, \psi^-)$  and a real scalar singlet  $\phi$  in addition to the SM particles. To achieve the stability of the dark sector, both the new fields are odd under  $\mathbb{Z}_2$  symmetry whereas the SM fields are  $\mathbb{Z}_2$ -even. In Table I the quantum number assignments of the particles relevant to new interactions are shown.

	$\ell_L$	$e_R$	$H$	$\Psi$	$\phi$
$SU(2)_L$	<b>2</b>	<b>1</b>	<b>2</b>	<b>2</b>	<b>1</b>
$U(1)_Y$	$-1/2$	$-1$	$1/2$	$-1/2$	$0$
$\mathbb{Z}_2$	$+$	$+$	$+$	$-$	$-$

TABLE I: Quantum number assignment of the relevant fields in our model. Electromagnetic charges are given by  $Q = t^3 + Y$ .

The real scalar singlet  $\phi$  which is our DM candidate interacts with the SM via the Higgs portal. As the other dark sector particles,  $(\psi^0, \psi^\pm)$  form an  $SU(2)_L$  doublet, it interacts with the SM through gauge bosons. Finally, the coannihilating doublet  $\Psi$  couples with the SM leptonic doublet  $\ell_L$  and the scalar singlet  $\phi$  via a Yukawa interaction. This is novel in the sense that the widely used Yukawa structure in any new physics model consists of a scalar doublet which is the replica of the SM Yukawa interaction. Although this particular Yukawa structure is less explored in the literature, it fits the bill for all our requirements for this study.

Hence the resulting Lagrangian takes the form

$$\mathcal{L} = \mathcal{L}_{\text{SM}} + \bar{\Psi} i \not{D} \Psi - \bar{\Psi} M_\Psi \Psi + \frac{1}{2} (\partial_\mu \phi)^2 - \frac{\mu_\phi^2}{2} \phi^2 - \frac{\lambda_\phi}{4} \phi^4 - \frac{\lambda_{h\phi}}{2} (H^\dagger H) \phi^2 - \sum_\alpha \left[ y_\alpha (\bar{\ell}_{\alpha L} \Psi) \phi + \text{h.c.} \right], \quad (1)$$

<sup>1</sup> Non-observance of any new fermionic partner state in LEP2 which interacts with the SM leptons via Yukawa type interaction puts a bound of  $m_\psi > 104$  GeV on their masses. However, please note that here the new fermions only interact strongly with  $\tau$ -lepton. Since LEP2  $\tau$  detection was not very precise, we must take this limit with a pinch of salt.

where  $\mathcal{L}_{\text{SM}}$  is the SM Lagrangian,  $M_\psi = \text{diag}(m_{\psi^0}, m_{\psi^\pm})$ , is the diagonal mass matrix and  $D_\mu = \partial_\mu + i g_W t^a W^a + i g' Y B_\mu$  is the covariant derivative of the fermionic doublet  $\Psi$ . The mass of the scalar singlet  $\phi$  is given by  $m_\phi^2 = \mu_\phi^2 + \lambda_{h\phi} v^2/2$ .

A discussion is in order here on the existing bounds that constrain the model parameters. The couplings which will play a significant role in the DM dynamics are the Higgs portal coupling  $\lambda_{h\phi}$  and the Yukawa couplings  $y_\ell, \ell = e, \mu, \tau$ . To put the bounds from the direct detection searches at bay we have considered  $\lambda_{h\phi} \lesssim 10^{-4}$  which also takes care of the invisible decay measurement. On the other hand, the muon  $g - 2$  measurement put the value of the Yukawa couplings of light leptons at  $y_e \sim y_\mu \lesssim 10^{-9}$ . This leaves the third generation Yukawa coupling  $y_\tau$  to be the only one free from experimental constraints. However, one must note that to keep our model in the perturbative regime, we must have  $y_\tau \leq 4\pi$ .

### III. DARK MATTER PHENOMENOLOGY

#### A. Formalism

In the proposed model, DM number changing processes are (i) pair annihilation ( $\phi\phi \rightarrow \text{SM SM}$ ), (ii) coannihilation ( $\phi\psi^{\pm 0} \rightarrow \text{SM SM}$ ) and (iii) mediator annihilation ( $\psi^{\pm 0}\psi^{\mp 0} \rightarrow \text{SM SM}$ ). The choice of parameters will determine the relative contribution of these processes towards the relic density as we discuss in the following sections. In agreement with the common assumption of thermal freeze-out, the dark sector particles are in equilibrium with the thermal bath in the early Universe. At the same time, they are also in chemical equilibrium with each other, due to substantial interaction strength between themselves. Keeping all these in mind, one can write the Boltzmann equation as follows [27]

$$\frac{dn}{dt} = -3Hn - \langle \sigma_{\text{eff}} v \rangle (n^2 - n_{\text{eq}}^2), \quad (2)$$

where  $n$  and  $n_{\text{eq}}$  are the DM number density and the equilibrium number density respectively. Now, the effective velocity averaged annihilation cross-section,  $\langle \sigma_{\text{eff}} v \rangle$  specific to this model can be written as

$$\begin{aligned} \langle \sigma_{\text{eff}} v \rangle = & \frac{1}{[g_\phi + \bar{g}_{\psi^0} + \bar{g}_{\psi^\pm}]^2} \left[ g_\phi^2 \langle \sigma_{\phi\phi \rightarrow \text{SM SM}} v \rangle + g_\phi \bar{g}_{\psi^0} \langle \sigma_{\phi\psi^0 \rightarrow \text{SM SM}} v \rangle \right. \\ & + g_\phi \bar{g}_{\psi^\pm} \langle \sigma_{\phi\psi^\pm \rightarrow \text{SM SM}} v \rangle + \bar{g}_{\psi^0}^2 \langle \sigma_{\psi^0\psi^0 \rightarrow \text{SM SM}} v \rangle + \bar{g}_{\psi^\pm}^2 \langle \sigma_{\psi^\pm\psi^\pm \rightarrow \text{SM SM}} v \rangle \\ & \left. + \bar{g}_{\psi^\pm} \bar{g}_{\psi^0} \langle \sigma_{\psi^\pm\psi^0 \rightarrow \text{SM SM}} v \rangle \right] \end{aligned} \quad (3)$$

where

$$\begin{aligned} \bar{g}_{\psi^0} &= g_{\psi^0} (1 + \Delta m_0)^{3/2} \exp[-x \Delta m_0], \\ \bar{g}_{\psi^\pm} &= g_{\psi^\pm} (1 + \Delta m_{\text{ch}})^{3/2} \exp[-x \Delta m_{\text{ch}}]. \end{aligned} \quad (4)$$

In the expressions above,  $g_\phi = 1$ ,  $g_{\psi^0} = g_{\psi^\pm} = 2$  are the internal degrees of freedom and  $x = m_\phi/T$ .  $\Delta m$ 's are dimensionless mass splitting parameters defined as

$$\begin{aligned} \Delta m_0 &= (m_{\psi^0} - m_\phi)/m_\phi, \\ \Delta m_{\text{ch}} &= (m_{\psi^\pm} - m_\phi)/m_\phi. \end{aligned} \quad (5)$$

As previously mentioned, the pair annihilation and coannihilation channels predominantly control the DM freeze-out. The mass splitting between  $\phi$  and other dark sector particles and the Yukawa couplings mainly determine the contribution of these processes towards the total DM annihilation cross-section. These mass splits, play a very important role, especially for the coannihilation and mediator annihilation processes as the Boltzmann factor in Eq. (3) gives rise to significantly increased annihilation cross-section for small values of  $\Delta m$ 's.

Before we go into the details of the freeze-out mechanisms, let us discuss the parameters used in the analysis. Since the mass splitting parameters defined in Eq. (5) between DM and other dark sector particles play an important role in freeze-out of  $\phi$ , we will use them as independent parameters along with DM mass. As discussed in the previous section, the only important Yukawa coupling here will be  $y_\tau$ , which couples  $\phi$  to the third generation  $SU(2)_L$  lepton doublet and the new fermionic doublet  $\Psi$ . In summary, we take the following values of the parameters throughout our analysis,

Free parameters: $m_\phi, \Delta m_0, \Delta m_{\text{ch}}, y_\tau,$ Fixed parameters: $\lambda_{h\phi} = 10^{-4}, y_e \sim y_\mu \sim 10^{-9}.$	(6)
---	-----

## B. Analysis and observations

### 1. Relic density

In addition to the Higgs portal annihilation channels of scalar singlet DM, the present model introduces a Yukawa interaction between the dark sector particles and SM. Unlike the Higgs-DM quartic coupling ( $\lambda_{h\phi}$ ), the new Yukawa coupling ( $y_\tau$ ) is unconstrained except for the perturbative limits. This provides an excellent tool to explain the relic density for a wide parameter space even with negligible  $\lambda_{h\phi}$ , which in turn alleviates the direct search bounds. We have performed DM analysis using micrOMEGAs [44].

Due to minuscule  $\lambda_{h\phi}$ , the Higgs portal annihilation channels have a negligible contribution towards DM relic density and hence we will focus on the newly introduced channels only. All these annihilation channels can be broadly classified into 3 categories:

- Pair annihilation ( $\phi\phi \rightarrow \text{SM SM}$ ) (Fig. 1)
- Coannihilation ( $\phi\psi^{\pm 0} \rightarrow \text{SM SM}$ ) (Fig. 2)
- Mediator annihilation ( $\psi^{\pm 0}\psi^{\mp 0} \rightarrow \text{SM SM}$ ) (Fig. 3)

All these categories can coexist or supersede each other, depending on the choice of parameters. As obvious from the figures below as well Eq. (3), the two  $\Delta m$ 's account for the strength of the coannihilation and mediator annihilation channels for two heavier dark sector particles  $\psi^0$  and  $\psi^\pm$ . Apart from this, the Yukawa coupling  $y_\tau$  also plays a significant role. In this context, it is worth noting that for the pair annihilation channels in Fig. 1, the cross-section depends on  $y_\tau^4$  while for coannihilation channels, it is only a  $y_\tau^2$  dependence and the mediator annihilation channels, being mostly gauge mediated, has a very little dependence on  $y_\tau$ . One can easily verify this from the analytical expressions in Eqs. (A1) and (A2).

Since all the above three categories of DM annihilation can coexist in the parameter space, it would be interesting to identify the limiting cases where the transition from one category to another is perceivable. It is worth mentioning here that the interaction channels between  $\phi$  and two other dark sector particles are exactly similar (see Figs. 1 and 2), so in the degenerate mass limit,  $m_{\psi^0} \sim m_{\psi^\pm}$ , their contribution will be the same. Hence, to see the effect of their interaction with DM, it is sufficient to take one  $\Delta m$  small and fix the other at large values so that the large propagator suppression in Fig. 1 or Boltzmann suppression in Fig. 2 practically makes the relevant channels negligible. In Fig. 4, the above mentioned transition is depicted in the  $y_\tau$  vs.  $m_\phi$  plane for some fixed values of  $\delta m = m_{\psi^\pm} - m_\phi$ .  $m_{\psi^0}$  is fixed at a much larger value (2 TeV) than  $m_{\phi_{\text{max}}}$  so that only  $\phi - \psi^\pm$  interactions are important.

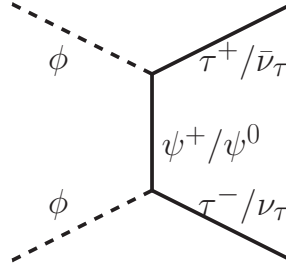


FIG. 1: Feynman diagrams depicting the pair annihilation channels of  $\phi$

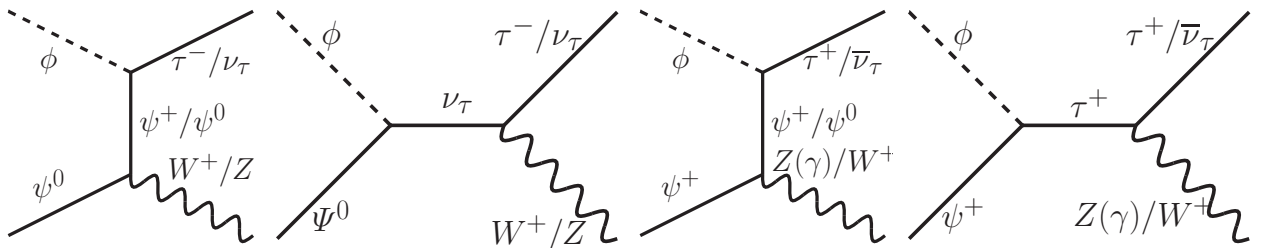


FIG. 2: Feynman diagrams depicting the coannihilation channels of  $\phi$

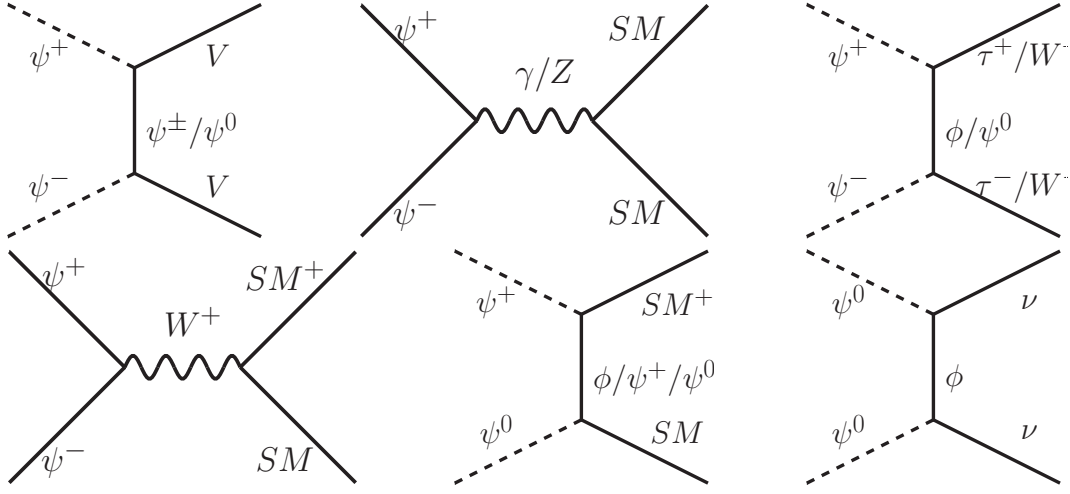


FIG. 3: Feynman diagrams depicting the mediator annihilation channels

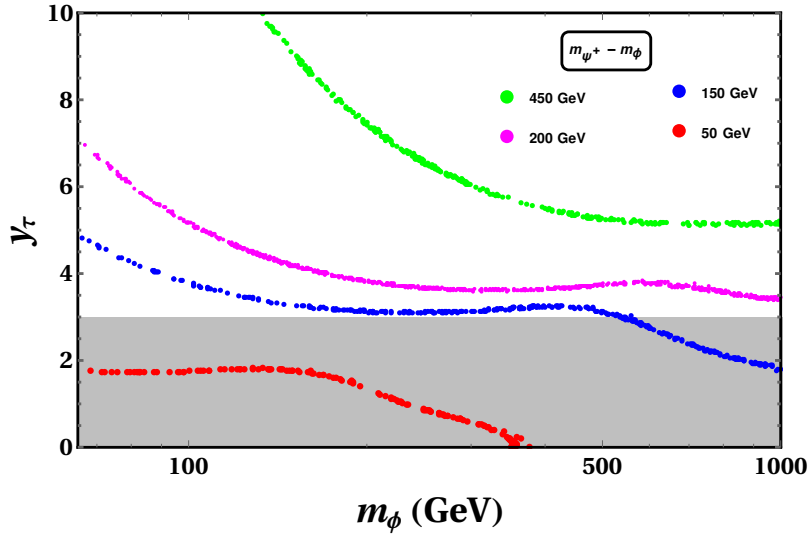


FIG. 4:  $y_\tau$  vs.  $m_\phi$  variation showing the transition from pair annihilation to coannihilation regime for different values of  $m_{\psi^+} - m_\phi$ .  $m_{\psi^0}$  is fixed at 2 TeV to avoid  $\psi^0$  contribution to relic density. The shaded region depicts the allowed region with  $y_\tau$  within the perturbative limits.

For pair annihilation,  $\langle\sigma_{\text{eff}}v\rangle$  has  $m_{\psi^\pm}$  dependence only in the  $t$ -channel propagator, but for coannihilation,  $m_{\psi^\pm}$  appears in the propagator and the initial state along with the Boltzmann factor (Eq. (4)). Now, for a very large value of  $\delta m$ , the coannihilation processes will be negligible due to substantially large Boltzmann suppression, and so the pair annihilation will predominantly dictate the DM annihilation. For these channels also, due to large propagator suppression, to obtain sufficient annihilation cross-section for the right relic, one has to go to very large coupling. This feature is clear from the green line in Fig. 4. For the magenta line, however, since the split is comparatively smaller, one can see an immediate effect in the reduction of the corresponding coupling.

However, an interesting feature is rather around a higher mass range of  $m_\phi$  where one can see that for a fixed value of  $m_\phi$ ,  $y_\tau$  is falling more sharply as we decrease the mass split. This is attributed to the exponential factor in the expression of  $\langle\sigma_{\text{eff}}v\rangle$  for coannihilation channels (Eq. (3)). For a fixed  $\delta m$ , larger  $m_\phi$  in this factor will make  $\langle\sigma_{\text{eff}}v\rangle$  more enhanced because of  $e^{-\delta m/m_\phi}$  and hence, to obtain right relic,  $y_\tau$  has to decrease. This feature is gradually prominent as we decrease the mass split because of stronger dependence on the exponential factor, e.g. in the red line, the exponential tail is visible even for a smaller value of  $m_\phi$  than the rest of the cases. However, it is important to mention that only for demonstration purposes, we have taken  $y_\tau$  up to 10. To stay well within perturbative limits, throughout our analysis, we have fixed the upper limit on  $y_\tau$  at 3. For convenience, we have shaded the allowed parameter space in the figure. From this constraint,

however, one can get a limit on the maximum range of the mass splits between  $\phi$  and  $\psi^\pm$  while  $m_\phi$  is varied over the entire range. But the more realistic picture will be for the case where both  $\psi^0$  and  $\psi^\pm$  vary instead of fixing one.

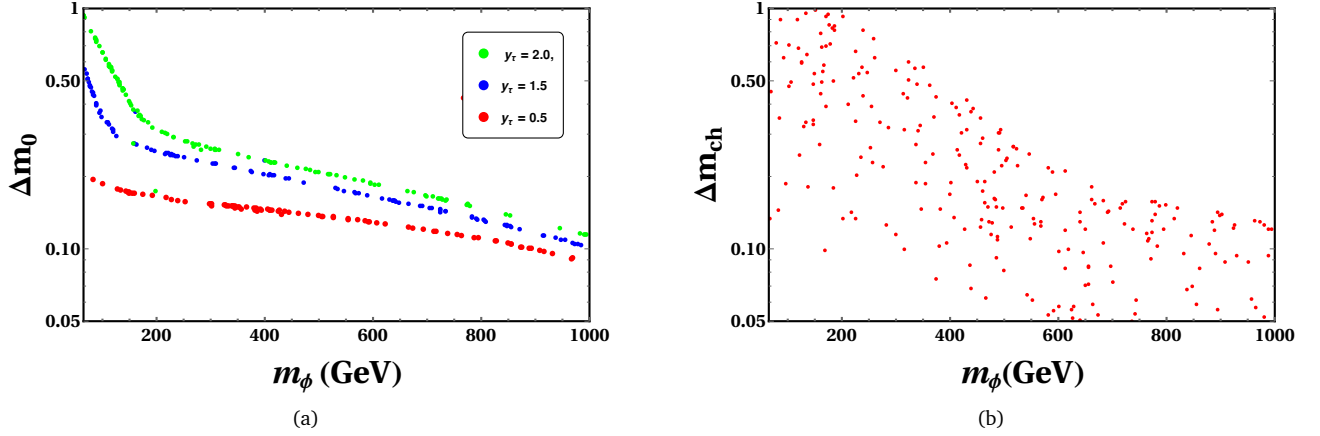


FIG. 5:  $\Delta m_0/\Delta m_{\text{ch}}$  vs.  $m_\phi$  variation for fixed values of  $y_\tau$  in the *left* plot and  $y_\tau$  varying within the allowed range in the *right* plot. All points satisfy relic density.

In Fig. 5a, the variation of  $\Delta m_0$  vs.  $m_\phi$  is plotted for all points satisfying right relic. The mass splitting between  $\phi$  and  $\psi^\pm$  is fixed at 100 GeV to rule out significant contribution from  $\phi\psi^\pm$  coannihilation channels. Major share in relic density comes from  $\phi\psi^0 \rightarrow \tau^\pm W^\mp$  and  $\phi\psi^0 \rightarrow \nu_\tau Z$  channels provided those are kinematically allowed. Larger values of  $\Delta m_0$  causes Boltzmann suppression in  $\langle\sigma_{\text{eff}}v\rangle$ , which in turn is compensated by larger values of the coupling, as clearly seen in the plot. However, this feature is more prominent for smaller values of  $m_\phi$ , as for a fixed  $\Delta m_0$ , larger values of  $m_\phi$  imply large  $m_{\psi^0} - m_\phi$  which rules out any substantial effect from the coannihilation channels. In Fig. 5b, a similar variation is observed between  $\Delta m_{\text{ch}}$  and  $m_\phi$  which shows the effect of the  $\phi\psi^\pm$  coannihilation channels. These channels include  $\phi\psi^\pm \rightarrow \tau^\pm Z/\gamma$ ,  $\phi\psi^\pm \rightarrow \nu_\tau W^\mp$  (see Fig. 2) and  $\phi\psi^\pm \rightarrow h\tau^\pm$ . The last one, however, will have very negligible contribution due to tiny  $h\tau\tau$  coupling.  $m_{\psi^0} - m_\phi$  is again fixed at 100 GeV to avoid large  $\phi\psi^0$  coannihilation contribution. However, unlike Fig. 5a, here  $y_\tau$  is varied over the entire range, ie, from 0 to 3.

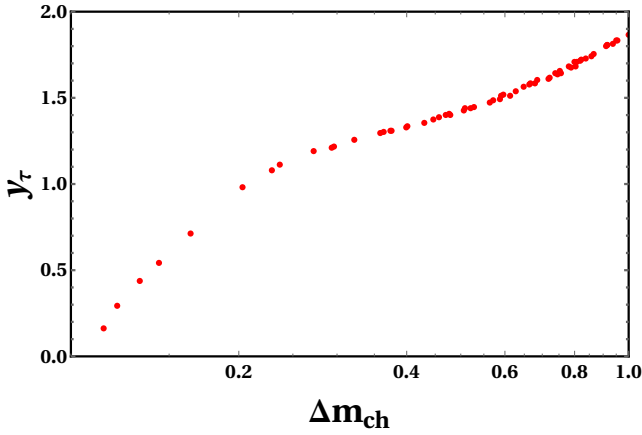


FIG. 6: Variation of relic density allowed points in  $y_\tau$  vs.  $\Delta m_{\text{ch}}$  plane for  $m_\phi=100$  GeV,  $m_{\psi^0}=250$  GeV. The coupling gradually increases for larger  $\Delta m_{\text{ch}}$  compensating for larger Boltzmann suppression in  $\langle\sigma_{\text{eff}}v\rangle$ .

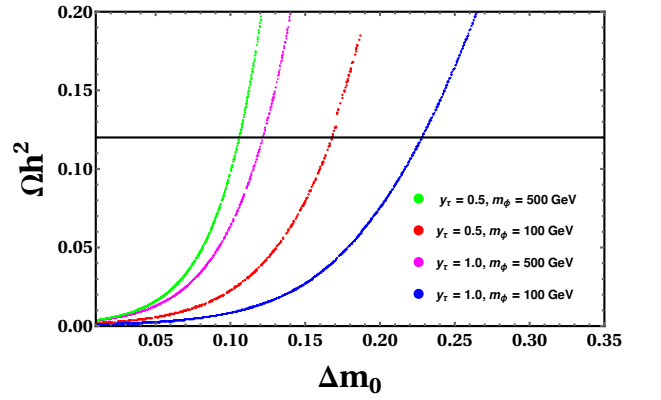


FIG. 7: Variation of relic density with  $\Delta m_0$  in the coannihilation regime for fixed values  $y_\tau$  and  $m_\phi$ . The black line represents right relic density at  $\Omega h^2 = 0.1215$ .

As mentioned previously, for very small values of  $\Delta m$ 's, the freeze-out of  $\psi^0$  and  $\psi^\pm$  also contributes to the relic density of  $\phi$ . This annihilation process is mediator driven. However, as observed from Eq. (3), the dependence on  $\Delta m$ 's is stronger in the Boltzmann factor of  $\langle\sigma_{\text{eff}}v\rangle$  than coannihilation. This leads to the fact that for very small values of  $\Delta m$ 's, the mediator driven annihilations almost entirely dominate the total DM annihilation. It is also worth noting that being mostly gauge mediated these channels substantially contribute to the DM annihilation even for very small values of  $y_\tau$ . For our choice of

parameters, we have observed that mediator annihilation is effective for  $(m_{\psi^\pm 0} - m_\phi) \lesssim 5$  GeV and then the coannihilation processes take over. This feature is clear from Fig. 6 where we can see that the dependence on  $y_\tau$  is negligible for  $\Delta m_{\text{ch}} \lesssim 0.1$  and beyond that range, as  $\Delta m_{\text{ch}}$  increases, the required coupling also increases gradually.  $m_\phi$  and  $m_{\psi^0}$  are fixed at 100 and 250 GeV respectively.

In Fig. 7, the variation of the relic density is plotted with  $\Delta m_0$  for some fixed Yukawa couplings and DM mass. As already argued, for a fixed  $m_\phi$ , larger coupling corresponds to larger  $\Delta m_0$  due to Boltzmann suppression in  $\langle \sigma_{\text{eff}} v \rangle$  as well as larger mass suppression of  $\psi^0$  in the t-channel propagator of the coannihilation channels. This explains the shift along the X-axis from the red to the blue line where  $m_\phi$  is 100 GeV and the Yukawa coupling  $y_\tau$  varies from 0.5 to 1.0. We see the same trend for the green and magenta lines, but the amount of shift is relatively less. Because, in this case,  $m_\phi$  is larger (500 GeV), which automatically implies a fairly large splitting between  $m_{\psi^0}^0$  and  $m_\phi$  and consequently the coannihilation effect is not so prominent. We can argue that for a fixed value of  $y_\tau$  larger DM mass obtains the correct relic density with a relatively smaller  $\Delta m_0$ , hence the red line with  $m_\phi = 100$  GeV shifts left towards the green line with the same  $y_\tau$  but larger  $m_\phi = 500$  GeV. The same logic applies to the shift between the blue and the magenta line. This trend also agrees with Figs. 5a and 5b.  $m_{\psi^\pm}$  is fixed at 1 TeV to rule out the effect of the  $\phi\psi^\pm$  coannihilation channels. As expected, very small values of  $\Delta m_0$  gives underabundance for the choice of parameters due to a fairly large increase in the Boltzmann factor of Eq. (4).

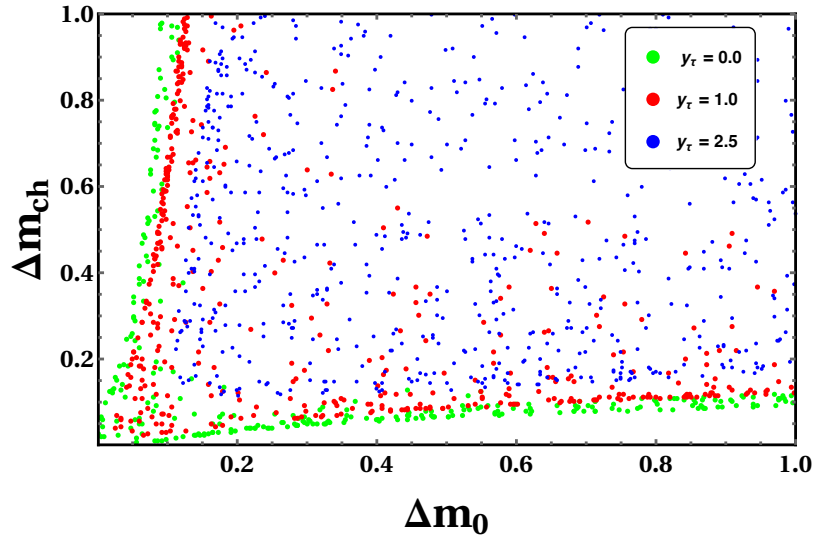


FIG. 8: Correlation between  $\Delta m_0$  and  $\Delta m_{\text{ch}}$  for different values of  $y_\tau$ .  $m_\phi$  varies from 65 GeV to 1 TeV. The three colors indicate the regions of parameter space where different DM number changing processes dictate the relic density.

Now we observe the possibility of coexistence of all the possible annihilation regimes by varying both  $\Delta m_0$  and  $\Delta m_{\text{ch}}$  along with the DM mass. Fig. 8 gives a correlation plot between  $\Delta m_0$  and  $\Delta m_{\text{ch}}$  at different values of  $y_\tau$ . For very small values of the coupling, mediator annihilation and coannihilation are dominant pair annihilation depending on  $\Delta m$ . Because as seen from Eqs. (A1) and (A2), annihilation cross-sections are proportional to  $y_\tau^4$  while for coannihilation it is only  $y_\tau^2$  and mediator annihilations are mostly gauge mediated. The green line, corresponding to  $y_\tau = 0.01$ , shows that one can obtain the correct relic density only if one of the  $\Delta m$ 's is fairly small. The red line, on the other hand, corresponding to a larger coupling ( $y_\tau = 1.0$ ), shows some scattered points in the allowed region. This implies that with the increase in the coupling, the pair annihilation channels become stronger and the Boltzmann suppression in  $\langle \sigma_{\text{eff}} v \rangle$  for larger mass splitting is compensated. The spread even increases for blue points, which corresponds to even larger  $y_\tau = 2.5$ . This implies that all three possible modes of annihilation can coexist in the present model for a wide parameter space where  $m_\phi$  varies from a few GeV up to the TeV scale and the coupling ranges from 0 to 3. Large Yukawa coupling and larger values of  $\Delta m_0$  and  $\Delta m_{\text{ch}}$  favour pair annihilation while the smaller values facilitate coannihilation and mediator annihilation.

## 2. Direct and indirect detection

- **Direct search prospect :** As known from the direct detection of scalar DM models, DM undergoes elastic scattering



with detector nuclei through Higgs mediation. The spin-independent scattering cross-section in our model is [45],

$$\sigma_{SI} = \frac{\lambda_{\phi h}^2}{16\pi m_h^4} f^2 \frac{m_N^4}{(m_\phi + m_N)^2} \quad (7)$$

where the form factor ( $f \sim 0.3$ ) contains all the contributions from the nuclear matrix elements. Throughout the study, we have fixed the DM-Higgs coupling  $\lambda_{\phi h}$  at  $10^{-4}$ . This keeps  $\sigma_{SI}$  well below the experimental bounds [46] as seen in Fig. 9. The new physics Yukawa coupling  $y_\tau$  being lepto-philic plays no role in direct searches. This is also quite clear from the plot.

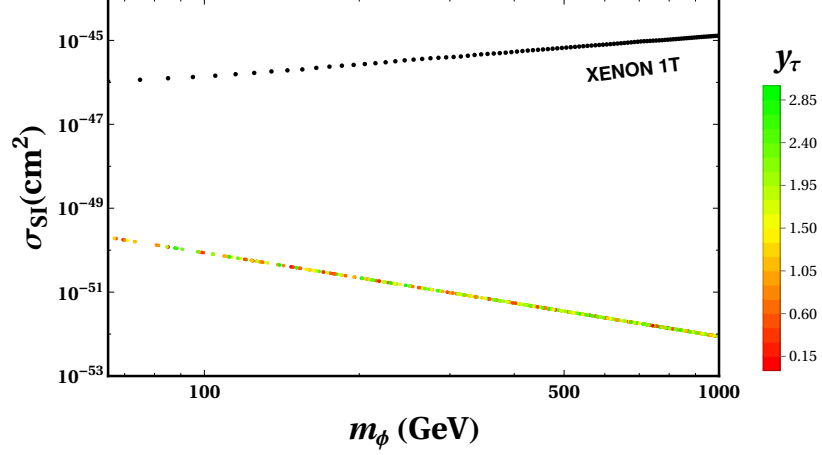


FIG. 9: Spin independent nuclear scattering cross-section ( $\sigma_{SI}$ ) vs.  $m_\phi$  plot indicating that the entire parameter space is safe from direct search limits.

- **Indirect search prospect :** The indirect detection experiments further constrain the DM velocity averaged cross-section for relevant channels contributing to high energy  $\gamma$  ray flux in the Universe. In the context of our model, as far as these possibilities are concerned, due to DM-Higgs coupling  $\lambda_{\phi h} = 10^{-4}$ ,  $\langle\sigma v\rangle_{\gamma\gamma}$  and  $\langle\sigma v\rangle_{b\bar{b}}$  contributions will be minuscule. However, the annihilation channels in Fig. 1 give rise to  $\langle\sigma v\rangle_{\tau^+\tau^-}$  possibility. In Fig. 10, we have varied  $m_\phi$  and  $y_\tau$  over the full range to check that the parameter space region considered remains safely below the experimental limits from Fermi-LAT data [16]. The larger  $\Delta m$ 's considered in Fig. 10b suggest larger propagator suppression for the relevant channels and consequently shift the parameter space downwards along the Y-axis compared to Fig. 10a, which is visible from the plots.

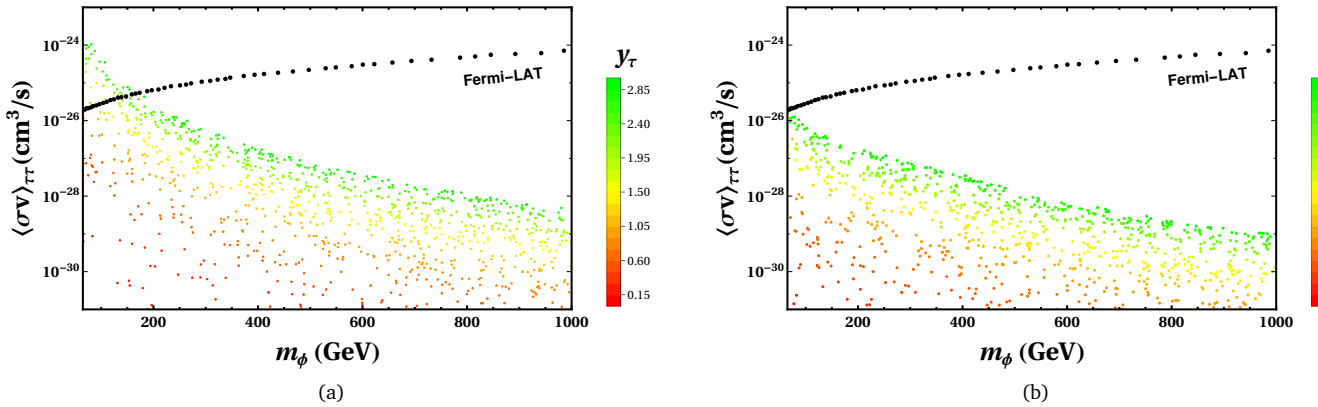


FIG. 10: Plots indicating that the entire parameter space is below the allowed bounds from  $\tau^+\tau^-$  measurements observed in Fermi-LAT.  $\Delta m_0 = \Delta m_{ch} = 0.01$  in the left panel and 1.0 in the right panel.



#### IV. COLLIDER SIGNATURES

The challenges of discovering dark matter in colliders are manifold. They manifest themselves as *missing energy* ( $E_T^{miss}$ ). Hence, the focus shifts entirely on the characteristics, and precise measurements of associated production of visible particles. The charged multi-lepton channels are the most suitable to probe dark matter because of its clean signal, whereas, QCD backgrounds overshadow the multi-jet channel, and it is very difficult to separate signals from the backgrounds. Here, we are going to study the collider signatures of DM through charged multi-lepton +  $E_T^{miss}$  channels. Our analysis will include both light charged leptons as well as  $\tau$ -leptons. We all know that  $\tau$ -leptons mostly decay hadronically and hence demand a separate analysis. Hence, in this section, we separately discuss both scenarios.

We have used FeynRules [47] to generate model files for our model. Events have been generated using MadGraph5 [48] and showered with Pythia 8 [49]. Finally, the detector simulation has been performed using Delphes [50]. We carried out our analysis for the LHC at the CM energy  $\sqrt{S} = 13$  TeV. We used the dynamic factorisation and renormalisation scale for the signal as well as the background events.

For the generation of parton-level events, we apply minimum or maximum cuts on the transverse momenta  $p_T$  and rapidities  $\eta$  of light jets,  $b$ -jets, leptons, photons, and missing transverse momentum. Also, distance cuts between all possible final objects in the rapidity-azimuthal plane are applied, with the distance between two objects  $i$  and  $j$  defined as  $\Delta R_{ij} = \sqrt{(\phi_i - \phi_j)^2 + (\eta_i - \eta_j)^2}$ , where  $\phi_i$  and  $\eta_i$  are the azimuthal angle and rapidity of the object  $i$ , respectively.

The preliminary selection cuts used in the analysis are:

- $p_T > 10$  and  $|\eta| < 2.5$  for all charged light leptons,
- $p_T > 20$  and  $|\eta| < 5$  for all *non- $b$* -jets, and
- $\Delta R_{ij} > 0.4$  between all possible jets or leptons.

After this, the .LHE files obtained through parton level events are showered with final state radiation (FSR) with Pythia 8 where initial state radiation (ISR) and multiple interactions are switched off and fragmentation/hadronization is allowed.

##### A. Analysis for the light di-lepton channel

In this channel the most important modes of production are

- (1)  $pp \rightarrow \ell^+ \ell^- 2\phi$  ;
- (2)  $pp \rightarrow \ell^+ \ell^- \nu \bar{\nu} 2\phi$  .

where, in general,  $\ell$  stands for all three generations of charged leptons, namely,  $e, \mu, \tau$ . We will take up the study of light di-lepton in this subsection and  $\ell$  will henceforth mean only  $e$  and  $\mu$  unless specifically mentioned. Please note the distinction between the signal process sets (1) and (2) as they will manifest themselves with more clarity in the studies of light- and  $\tau$ -leptons.

To highlight the features of our model clearly, we have selected the following benchmark points (see Table II). The significance of the choice in benchmark points will be clear as we elaborate on our analysis in the following subsections. For the benchmark points given in Table II we get the cross-sections as shown in Table III.

	$m_\phi$ (GeV)	$m_{\psi^0}$ (GeV)	$m_{\psi^\pm}$ (GeV)	$y_\tau$
BP1	200	350	300	2.2
BP2	100	125	120	0.7
BP3	80	100	90	0.1
BP4	70	100	170	1.23

TABLE II: Benchmark points used for the collider analysis.

Among the two classes of signal processes, the set (1) is subdominant. To understand its reason let us enumerate the subprocesses that take part in this.

- (i)  $pp \rightarrow \psi^+ \psi^-$ , followed by the decay of both  $\psi^\pm$  as  $\psi^\pm \rightarrow \ell^\pm \phi$  ;

Processes	cross-section (pb)			
	BP1	BP2	BP3	BP4
(1) $pp \rightarrow \ell^+ \ell^- 2\phi$	$\sim 10^{-36}$	$\sim 10^{-33}$	$\sim 10^{-33}$	$\sim 10^{-33}$
(2) $pp \rightarrow \ell^+ \ell^- \nu \bar{\nu} 2\phi$	$11.72 \times 10^{-6}$	$232.17 \times 10^{-6}$	$409.30 \times 10^{-6}$	$409.73 \times 10^{-6}$

TABLE III: Cross-sections of the light di-lepton signal processes. The set (1) of subprocesses are subdominant as they involve only couplings involving light leptons, whereas the set (2) further involves gauge and  $\tau$ -lepton couplings and hence are dominant in this scenario.

The couplings which play a role in the above processes are only the ones involving light leptons and hence are very suppressed as shown in Eq. (6).

On the other hand, the set (2) of processes mentioned above will proceed as

- (i)  $pp \rightarrow \psi^0 \bar{\psi}^0$ , followed by  $\psi^0 \rightarrow \phi \nu$  and  $\bar{\psi}^0 \rightarrow \ell^+ \ell^- \bar{\nu} \phi$ .
- (ii)  $pp \rightarrow W^+ W^-$ , followed by  $W^+ \rightarrow \ell^+ \nu$  and  $W^- \rightarrow \ell^- \nu 2\phi$ .
- (iii)  $pp \rightarrow \psi^+ \psi^-$ , followed by  $\psi^+ \rightarrow \ell^+ \nu$  and  $\psi^- \rightarrow \ell^- \nu 2\phi$ .
- (iv)  $pp \rightarrow ZZ(\gamma^*)$ , followed by  $Z \rightarrow \nu \bar{\nu} 2\phi$  and  $Z(\gamma^*) \rightarrow \ell^+ \ell^-$ .

As the couplings involved can also be either gauge couplings or that involving  $\tau$ -lepton, both being considerably large, the set (2) of processes give us sufficient cross-sections to proceed with our analysis. This is clear from Table III.

The major backgrounds at the LHC for the light di-lepton channel are as follows

**Bkg1** :  $pp \rightarrow t \bar{t}$ , followed by the top (anti-)quark decaying into the leptonic channel,  $t(\bar{t}) \rightarrow \ell^\pm \nu(\bar{\nu}) b(\bar{b})$ .

**Bkg2** :  $pp \rightarrow W^+ W^-$ .  $W^\pm$  further decays via leptonic channel as  $W^\pm \rightarrow \ell^\pm \nu(\bar{\nu})$ .

**Bkg3** :  $pp \rightarrow W^\pm Z(\gamma^*)$ , followed by  $W^\pm \rightarrow \ell^\pm \nu(\bar{\nu})$ , and  $Z/\gamma^*$  decays into leptonic channel,  $Z(\gamma^*) \rightarrow \ell^+ \ell^-$ .

**Bkg4** :  $pp \rightarrow ZZ(\gamma^*)$ , followed by leptonic decays  $Z \rightarrow \nu \bar{\nu}$  and  $Z(\gamma^*) \rightarrow \ell^+ \ell^-$ .

Table IV shows the cross-sections for the above backgrounds.

Processes	cross-section [pb]
<b>Bkg1</b>	21.27
<b>Bkg2</b>	3.13
<b>Bkg3</b>	$402.68 \times 10^{-3}$
<b>Bkg4</b>	$272.43 \times 10^{-3}$

TABLE IV: cross-sections of the leptonic backgrounds.

Before getting involved in more intricate analysis, we shall first discuss the kinematic distributions for this channel. The kinematic observables at our disposal are only the 4-momenta of the leptons and the missing energy  $E_T^{miss}$ . We order them according to the magnitude of their transverse momentum  $p_T$ . As a result, a *leading lepton* would always mean the leading- $p_T$  lepton. We can also construct other observables from them, such as the invariant mass of the lepton pair. In a similar vein, we would construct the so-called transverse mass of the lepton- $E_T^{miss}$  system. We shall call this quantity the missing transverse mass and define it for each lepton- $E_T^{miss}$  system as

$$M_{T\ell}^{miss} = \sqrt{2 E_T^\ell E_T^{miss} (1 - \cos \Delta\phi_{\ell E_T^{miss}})}, \quad (8)$$

where  $E_T^\ell = p_T^\ell$ , which is the magnitude of the transverse momentum of a given lepton and  $\Delta\phi_{\ell E_T^{miss}}$  is the difference between the azimuthal angles of the lepton and missing transverse momentum. The missing transverse mass plays an important role in distinguishing the massless invisible particles (such as neutrinos) from the massive ones (as is the case for our dark matter candidates) and hence is very crucial for our analysis. In Fig. 11, we show some of the distributions for this channel.

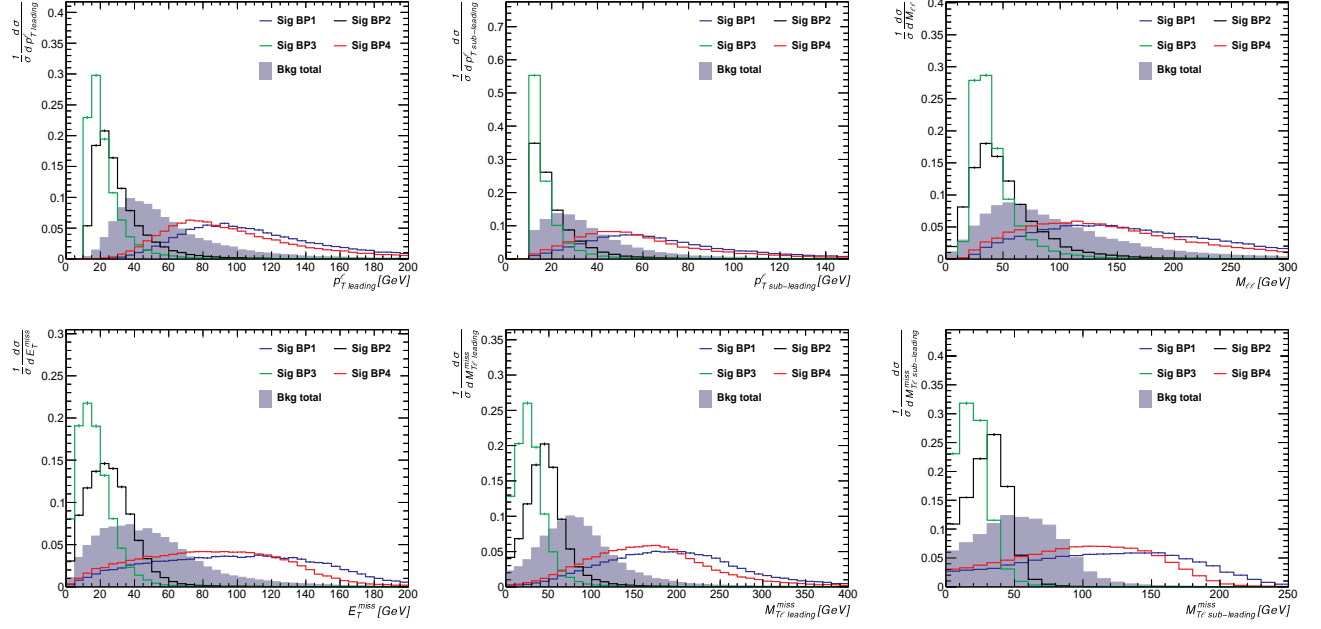


FIG. 11: Distribution plots for the di-lepton channel. The top panel shows  $p_T$  distributions of the leading and sub-leading  $p_T$ -ordered leptons and the lepton invariant mass. The bottom panel shows the distributions of the missing transverse energy, missing transverse masses with leading and sub-leading leptons.

Before going further into the analysis, let us discuss the features of the benchmark points which we mentioned previously. It is clear from the distributions that the benchmark points 1 and 4 have similar patterns, whereas 2 and 3 are similar. For the first case, the distributions are more populated in the lower region of each observable. On the other hand, the distributions are more populated in the higher values for the latter case.

In the next level of our study, we use Toolkit for Multivariate Data Analysis (TMVA) [51] in ROOT, to distinguish the signal events from the backgrounds efficiently. For this, we use the distributions of Fig. 11 and some other kinematic observables to train a boosted decision tree (BDT). The complete list of observables used to train BDT are as follows:

- $p_T$  and  $\eta$  of the leading and sub-leading leptons and the invariant mass of the pair.
- missing transverse momentum  $E_T^{\text{miss}}$ .
- missing transverse mass  $M_T^{\text{miss}}$  of the leading and sub-leading leptons.
- the difference of the azimuthal angles  $\Delta\Phi_{\ell E_T^{\text{miss}}}$  of the leading and sub-leading leptons with the missing transverse energy.

We use these distributions as discriminators to the BDT analysis. The discrimination of the signal and background can be improved further using proper cuts in addition to the preliminary selection cuts to the signal and/or background events. The resulting BDT-response functions give us an estimate of the signal efficiency vs. the rejection of the background.

Fig. 12 shows the BDT-response curves (solid filled histograms are for the signal and the hollow ones are for the background) for the di-lepton channel for each benchmark points. Here we show two sets of BDT-responses: (1) the solid purple and the hollow red ones are before any additional cuts with only taking into account the preliminary selection cuts, whereas (2) the solid blue and the hollow black ones are after implementing carefully chosen additional set of cuts to improve the distinguishability of the signal from the backgrounds. We will elaborate on the cuts chosen later on in this subsection.

We observe that the signal is separable from the background from the BDT-response curves of Fig. 12 after the use of additional cuts. However, we have not yet quantified the improvement. For this, we draw the *Receiver Operating Characteristic* (ROC) curves for each benchmark point using the gradual use of additional cuts. Fig. 13 shows the resulting curves for the signal efficiency vs. the rejection of the background. The area under each curve gives the quantitative estimate of the goodness of the separation of the signal from the backgrounds. The inset of Fig. 13 shows the area under the ROC curve for each cut. The value of the cut is in addition to all the preceding cuts. We can see the improvement in the separation of the signal from the backgrounds from these numbers. This feature is consistent with that of Fig. 12. The important point to be noted here is that the cuts were used only on the signal events for the benchmark points 1 and 4 leaving the background

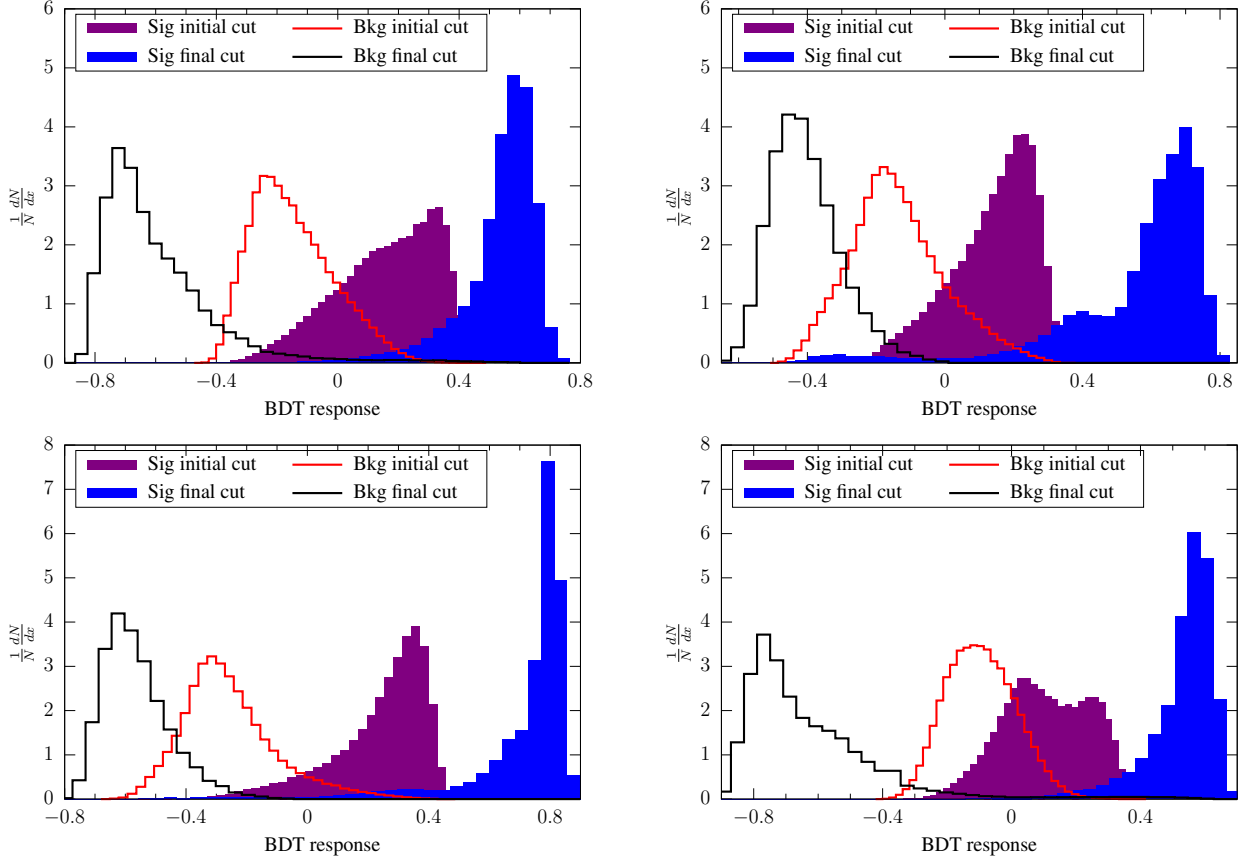


FIG. 12: BDT-response curves for the di-lepton channel. The top panel is for benchmarks 1 and 2, whereas the bottom panel shows the curves for benchmarks 3 and 4. The solid purple and the hollow red ones are before any additional cuts with only taking into account the preliminary selection cuts, whereas the solid blue and the hollow black ones are after implementing carefully chosen additional set of cuts.

events untouched, whereas the opposite has been done for the benchmark points for 2 and 3. The reason for this can be understood as the population of events in the distribution plots of Fig. 11.

### B. Analysis for the di- $\tau$ -jet channel

Although  $\tau$ -lepton analysis poses more challenges, at the same time it unravels more unique features that can come handy in the analysis for any collider like LHC. The  $\tau$ -lepton is the charged lepton of the third generation and the heaviest among them. It is even heavier than most of the light quark mesons. As a result,  $\tau$ -leptons decay hadronically, which sets it apart from all other leptons. Due to the lepton number conserving weak interactions, the  $\tau$  final states are always accompanied by one neutrino in the hadronic final states and two neutrinos in the leptonic final states. Since the neutrinos add to the missing energy, the full  $\tau$  energy cannot be measured. The leptonic decays of the  $\tau$  is difficult to distinguish from prompt leptons in a  $\ell + E_T^{\text{miss}}$  final state. Therefore only the hadronically decaying  $\tau$ 's are suitable for the collider signatures. We use the  $\tau$ -tagged jets from Delphes and reconstruct them with the help of FastJet [52] using anti- $k_T$  algorithm. The separation  $\Delta R$  of two adjacent  $\tau$ -jets is taken to be 0.4 and the  $\tau$ -tagging efficiency is taken to be 60%.

In this subsection, we will take up the discussion of  $\tau$ -jet channel. Here we follow the same line of analysis as the light di-lepton. As in the case above, here also the most important modes of production are

- (1)  $pp \rightarrow \tau^+ \tau^- 2\phi$  ;
- (2)  $pp \rightarrow \tau^+ \tau^- \nu \bar{\nu} 2\phi$  .

Contrary to the light di-lepton channel, the signal process set (1) here is more dominant than set (2) as mentioned previously. This is because although the large value of  $y_\tau$  and gauge couplings dictate both the processes, process (2) is suppressed by branchings and phase space.

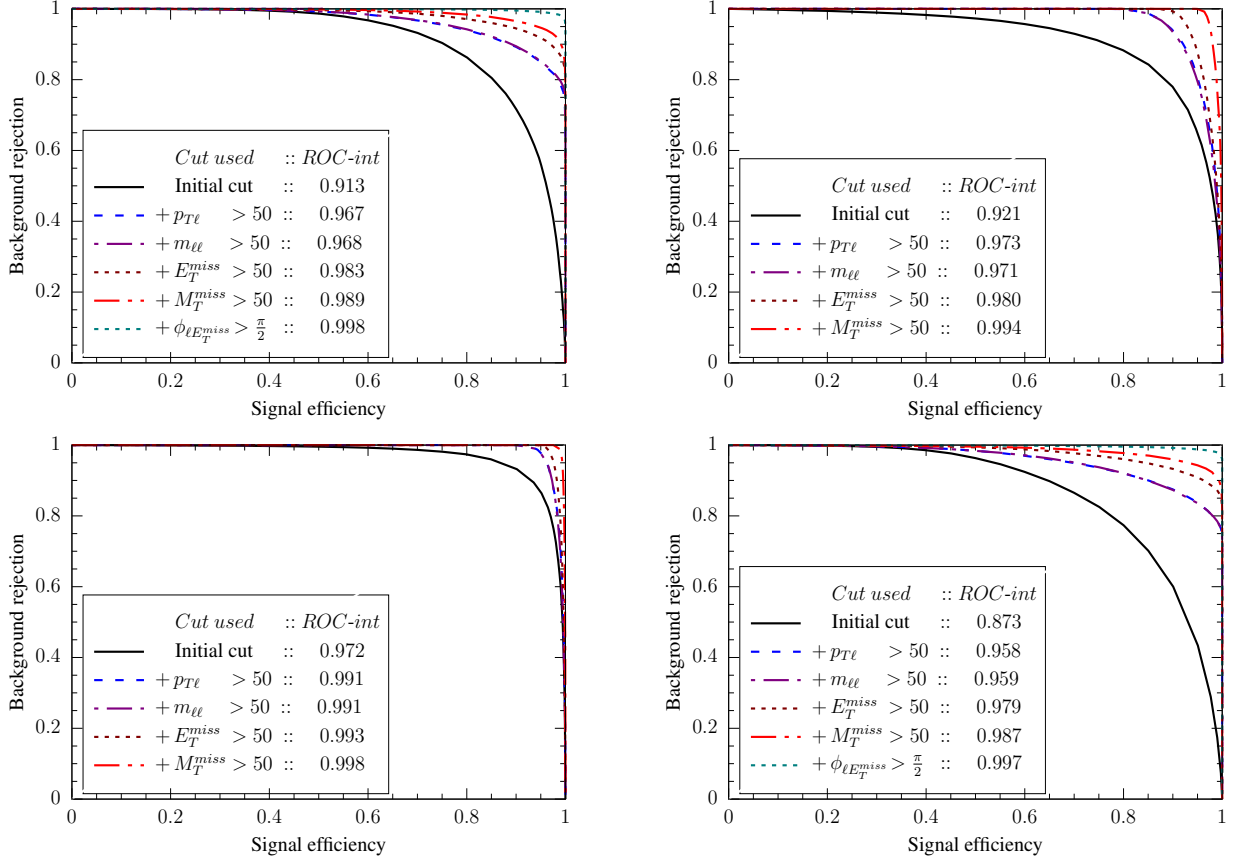


FIG. 13: ROC curves for the di-lepton channel. The top panel shows the curves for benchmarks 1 and 2, whereas the bottom panel for benchmarks 3 and 4. The area under the ROC curve for each cut is given in the inset. The value of the cut is in addition to all the preceding cuts.

Table V shows the signal cross-sections for di- $\tau$ -jet channel. As mentioned previously we can see the distinction between the cross-sections of process (1) which is substantially greater than that of process (2) for this case. This can be understood from the sub-processes enumerated in the previous subsection with  $\tau$  in the final states instead of light lepton.

Processes	cross-section (pb)			
	BP1	BP2	BP3	BP4
(1) $pp \rightarrow \tau^+ \tau^- 2\phi$	$38.64 \times 10^{-3}$	$805.09 \times 10^{-3}$	$786.33 \times 10^{-3}$	$325.75 \times 10^{-3}$
(2) $pp \rightarrow \tau^+ \tau^- \nu \bar{\nu} 2\phi$	$217.14 \times 10^{-6}$	$2.72 \times 10^{-3}$	$3.33 \times 10^{-3}$	$2.72 \times 10^{-3}$

TABLE V: Cross-sections of the signal processes for di- $\tau$ -jet channel.

The major backgrounds at the LHC for the  $\tau$ -jet channel are as follows

**Bkg1** :  $pp \rightarrow t\bar{t}$ , followed by the top (anti-)quark decaying into the  $\tau$ -jet channel,  $t(\bar{t}) \rightarrow \tau^\pm \nu(\bar{\nu}) b(\bar{b})$ .

**Bkg2** :  $pp \rightarrow W^+ W^-$ .  $W^\pm$  further decays via  $\tau$ -jet channel as  $W^\pm \rightarrow \tau^\pm \nu(\bar{\nu})$ .

**Bkg3** :  $pp \rightarrow W^\pm Z(\gamma^*)$ , followed by  $W^\pm \rightarrow \tau^\pm \nu(\bar{\nu})$ , and  $Z/\gamma^*$  decays into  $\tau$ -jet channel,  $Z(\gamma^*) \rightarrow \tau^+ \tau^- / 2j$ .

**Bkg4** :  $pp \rightarrow ZZ(\gamma^*)$ , followed by  $Z \rightarrow \nu \bar{\nu}$  and jet decays  $Z(\gamma^*) \rightarrow \tau^+ \tau^- / 2j$ .

Table VI shows the cross-sections for the above backgrounds.

Some relevant distributions for this channel is shown in Fig. 14. Similar to the light di-lepton case, here also we can distinguish the benchmark points 1 and 4 from those of 2 and 3.

Processes	cross-section [pb]
<b>Bkg1</b>	5.31
<b>Bkg2</b>	$781.43 \times 10^{-3}$
<b>Bkg3</b>	$14.75 \times 10^3$
<b>Bkg4</b>	$2.78 \times 10^3$

TABLE VI: cross-sections of the jet backgrounds.

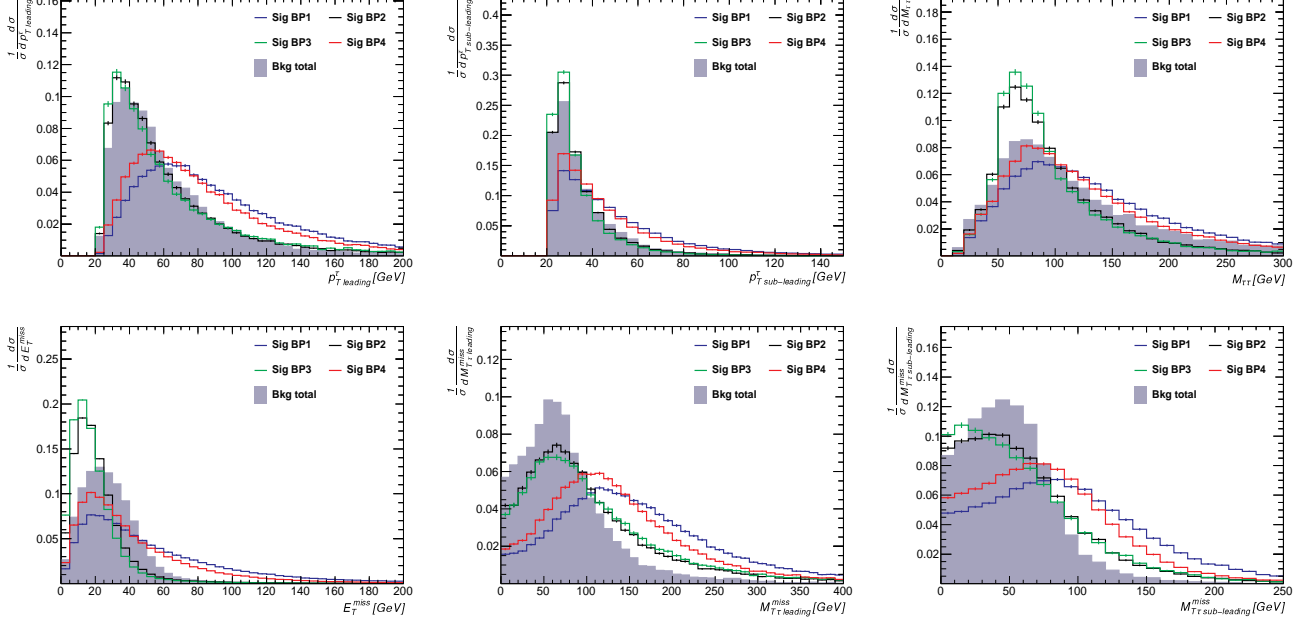


FIG. 14: Distribution plots for the di- $\tau$ -jet channel. The top panel shows  $p_T$  distributions of the leading and sub-leading  $p_T$ -ordered  $\tau$ -jets and the  $\tau$ -jet invariant mass. The bottom panel shows the distributions of the missing transverse energy, missing transverse masses with leading and sub-leading  $\tau$ -jets.

Next we use TMVA to distinguish the signal events from the backgrounds. The distributions used as the discriminator to train a BDT are as follows:

- $p_T$  and  $\eta$  of the leading and sub-leading  $\tau$ -jets and their invariant mass.
- missing transverse momentum  $E_T^{\text{miss}}$ .
- missing transverse mass  $M_T^{\text{miss}}$  of the leading and sub-leading  $\tau$ -jets.
- the difference of the azimuthal angles  $\Delta\Phi_{\tau E_T^{\text{miss}}}$  of the leading and sub-leading  $\tau$ -jets with the missing transverse energy.

Same as above, we use these distributions as discriminators to the BDT analysis and draw the BDT response curves. Fig. 15 shows the BDT-response curves (similar to the previous case, here also the solid filled histograms are for the signal and the hollow ones are for the background). Two sets of BDT-responses corresponds to: (1) the solid purple and the hollow red ones are before any additional cuts with only taking into account the preliminary selection cuts, whereas (2) the solid blue and the hollow black ones are after implementing carefully chosen additional set of cuts to improve the distinguishability of the signal from the backgrounds.

Fig. 16 shows the ROC curve for the signal efficiency vs. the rejection of the background. The inset of Fig. 16 shows the area under the ROC curve for each cut. As in the previous case, the value of the cut is in addition to all the preceding cuts. We can see the visible improvement in the separation of the signal from the backgrounds from these numbers. Please note that, unlike the previous case, here the cuts were used only on the signal events.

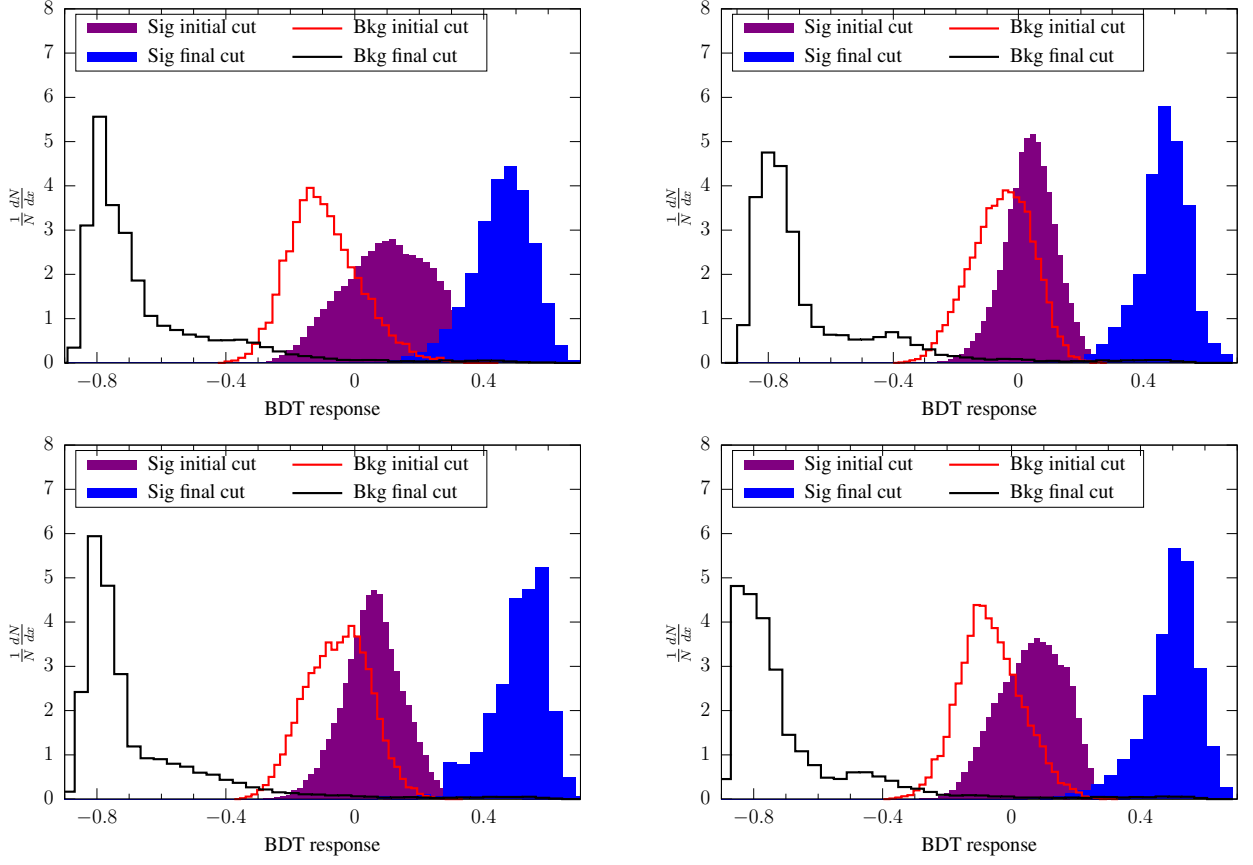


FIG. 15: BDT-response curves for the di- $\tau$ -jet channel. The top panel is for benchmarks 1 and 2, whereas the bottom panel shows the curves for benchmarks 3 and 4. The solid purple and the hollow red ones are before any additional cuts with only taking into account the preliminary selection cuts, whereas the solid blue and the hollow black ones are after implementing carefully chosen additional set of cuts.

## V. CONCLUSION

In this work, we have proposed a singlet scalar DM with a vector-like fermionic doublet having the same dark symmetry. The minuscule Higgs portal coupling with scalar DM keeps the direct detection cross-section below the experimental bound which is an important handle in reviving the scenario of scalar singlet DM models. The new Yukawa coupling, on the other hand, which is irrelevant to direct search prospects, plays a vital role in dictating the relic density. We have shown that the model can provide a viable DM candidate through pair annihilation, coannihilation, and mediator annihilation channels over a wide of parameter space ranging from GeV up to TeV scale. The transition from pair annihilation to coannihilation regime is demonstrated and the relevant limits of parameters are discussed. We have observed that coannihilation processes have a substantial contribution to relic density for a comparatively larger mass splitting between DM and the dark sector particles than what is usually discussed in the literature. This may be attributed to the gauge couplings involved in these channels which is a substantial contribution thanks to the dark fermion being a doublet. This is an artifact of the unconventional BSM Yukawa structure considered in the proposed model. This arrangement, involving SM and dark sector lepton  $SU(2)_L$  doublets and a scalar singlet appropriately highlights the important features in the work.

Apart from the DM context, the gauge production of the fermionic doublet followed by decay to DM through the Yukawa coupling results in a substantially increased DM production at the colliders compared to scalar singlet scenarios. Using suitable kinematic observables in Boosted Decision Tree (BDT) classifier, we separate the signal events from the backgrounds in an effective manner. We have shown that with the use of proper cuts, we can achieve good results for both the light as well as  $\tau$  leptonic channels. This model can also provide potential search prospects for long-lived particles because for mediator annihilation and coannihilation regimes, the mass splittings between DM and other dark sector particles are typically considered to be very small. This can lead to suppressed decay width of the coannihilating partner and the delayed decay can facilitate long-lived signatures (LLP) in the colliders which is recently being given wide attention in the literature.

One can interpret a limitation of the proposed model in the sense that from the observed results in both dark matter and



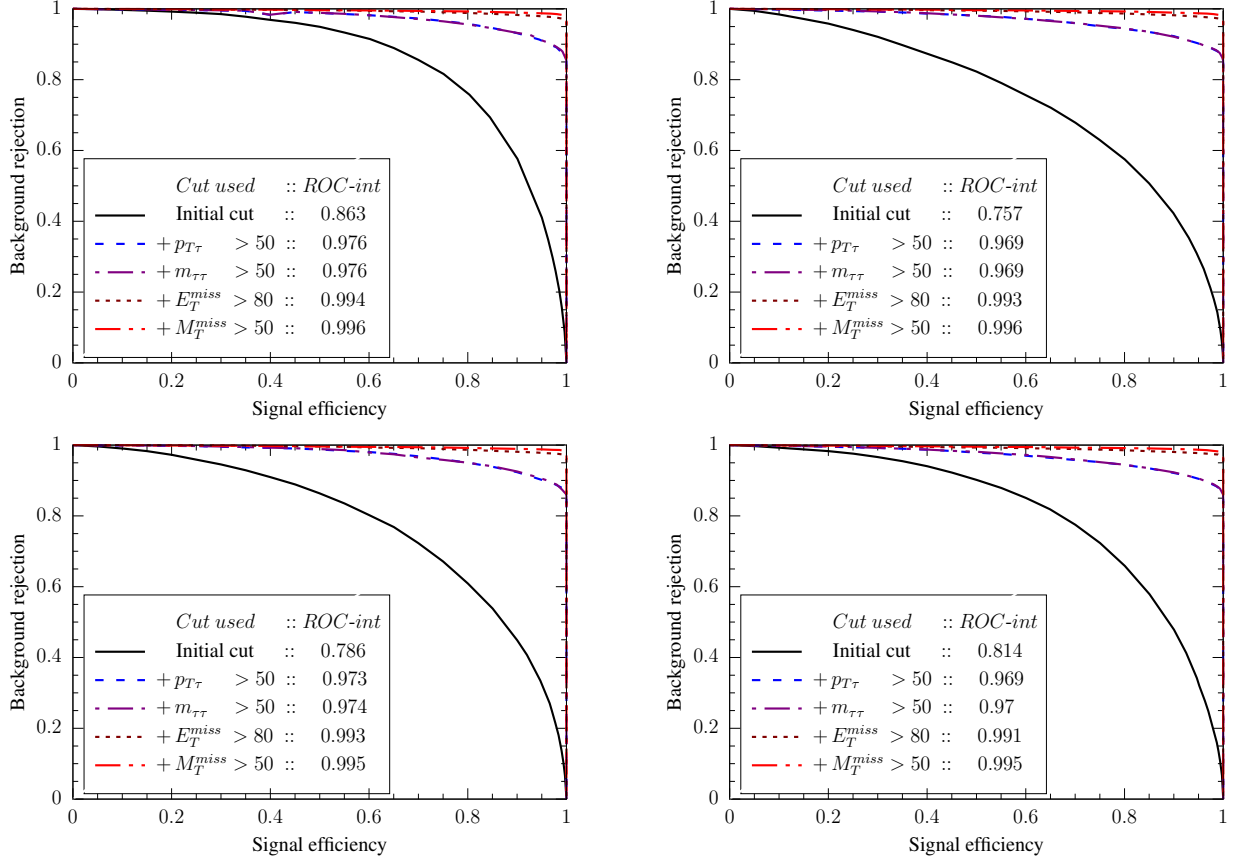


FIG. 16: ROC curves for the di- $\tau$ -jet channel. The top panel shows the curves for benchmarks 1 and 2, whereas the bottom panel for benchmarks 3 and 4. The area under the ROC curve for each cut is given in the inset. The value of the cut is in addition to all the preceding cuts.

the collider analysis, there is no way to distinguish between the two coannihilating partners. We are pursuing a possible solution to address this issue in an ongoing work.

### Appendix A: Appendix

Differential cross-section of the pair annihilation process  $\phi\phi \rightarrow \tau^+\tau^-$  is

$$\frac{d\sigma}{dc_\theta} = \frac{1}{32\pi} \frac{y_\tau^4}{4} \sqrt{s(s-4m_\phi^2)} (1-c_\theta^2) \left[ \frac{1}{(t-m_{\psi^+}^2)^2 + \Gamma_{\psi^+}^2 m_{\psi^+}^2} + \frac{1}{(u-m_{\psi^+}^2)^2 + \Gamma_{\psi^+}^2 m_{\psi^+}^2} - \frac{2}{\left[ (t-m_{\psi^+}^2)^2 + \Gamma_{\psi^+}^2 m_{\psi^+}^2 \right]^{\frac{1}{2}} \left[ (u-m_{\psi^+}^2)^2 + \Gamma_{\psi^+}^2 m_{\psi^+}^2 \right]^{\frac{1}{2}}} \right]. \quad (\text{A1})$$

In the above, we neglected the  $\tau$ -lepton mass. We will get the same expression for the process  $\phi\phi \rightarrow \nu_\tau \bar{\nu}_\tau$  with  $m_{\psi^+} \rightarrow m_{\psi^0}$  and  $\Gamma_{\psi^+} \rightarrow \Gamma_{\psi^0}$ . Differential cross-section of the pair annihilation process  $\phi\psi^0 \rightarrow \nu_\tau Z$  is

$$\begin{aligned}
\frac{d\sigma}{dc_\theta} = & \frac{1}{32s^{3/2}} \frac{s-m_Z^2}{p m_Z^2} \frac{y_\tau^2 \alpha_{EM}}{\sin^2 2\theta_W} \left[ \frac{1}{s^2} \left\{ p\sqrt{s}c_\theta (s-2m_Z^2)(s-m_Z^2) + \frac{1}{2} [(m_\phi^2 - m_{\psi^0}^2)(6m_Z^4 \right. \right. \\
& - 3m_Z^2s - s^2) + s(2m_Z^4 - m_Z^2s + s^2)] \left. \right\} + \frac{1}{(u-m_{\psi^0}^2)^2 + \Gamma_{\psi^0}^2 m_{\psi^0}^2} \left\{ \frac{p^3 c_\theta^3}{s^{3/2}} (s-m_Z^2)^3 \right. \\
& - \frac{p^2 c_\theta^2}{2s^2} (m_Z^2 - s)^2 [(m_\phi^2 - m_{\psi^0}^2)(3m_Z^2 - s) + s(5m_Z^2 + s)] - \frac{p c_\theta}{4s^{5/2}} (m_Z^2 - s) [(3m_Z^4 \\
& - 2m_Z^2s - s^2)(m_\phi^4 - 2m_\phi^2 m_{\psi^0}^2 + m_{\psi^0}^4) + 2m_\phi^2 s(5m_Z^4 - 2m_Z^2s + s^2) - 2m_{\psi^0}^2 s(5m_Z^4 \\
& + 6m_Z^2s + s^2) + s^2(7m_Z^4 - 2m_Z^2s - s^2)] - \frac{m_\phi^6}{8s^3} (m_Z^2 - s)^2 (m_Z^2 + s) \\
& - m_\phi^4 (m_Z^2 - s) (-3m_{\psi^0}^2 (m_Z^4 - s^2) + 5m_Z^4s + 3s^3) + m_\phi^2 (-3m_{\psi^0}^4 (m_Z^2 - s)^2 (m_Z^2 + s) \\
& + 2m_{\psi^0}^2 s(5m_Z^6 + 3m_Z^4s + 11m_Z^2s^2 - 3s^3) - s^2(7m_Z^6 - 23m_Z^4s + 5m_Z^2s^2 + 3s^3)) \\
& + m_{\psi^0}^6 (m_Z^2 - s)^2 (m_Z^2 + s) + m_{\psi^0}^4 s(-5m_Z^6 - 11m_Z^4s - 19m_Z^2s^2 + 3s^3) \\
& + m_{\psi^0}^2 s^2(7m_Z^6 - 7m_Z^4s + 21m_Z^2s^2 + 3s^3) + s^3(-3m_Z^6 + 3m_Z^4s + 7m_Z^2s^2 + s^3) \left. \right\} \\
& - \frac{2}{[(u-m_{\psi^0}^2)^2 + \Gamma_{\psi^0}^2 m_{\psi^0}^2]^{\frac{1}{2}}} \left\{ p^2 s c_\theta^2 (m_Z^2 - s)^2 + \frac{3p}{\sqrt{s}} m_Z^2 c_\theta (m_\phi^2 - m_{\psi^0}^2) (m_Z^2 - s) \right. \\
& + \frac{1}{4s} [(5m_Z^2 - s)(m_Z^2 + s)(m_\phi^4 - 2m_\phi^2 m_{\psi^0}^2 + m_{\psi^0}^4) + 2m_\phi^2 s(2m_Z^4 - m_Z^2s + s^2) \\
& \left. \left. - 2m_{\psi^0}^2 s(-2m_Z^4 + 3m_Z^2s + s^2) - s^2(m_Z^2 + s)^2 \right) \right\} \right]. \tag{A2}
\end{aligned}$$

With the substitution  $m_{\psi^+} \rightarrow m_{\psi^0}$ ,  $m_Z \rightarrow m_W$  and  $\Gamma_{\psi^0} \rightarrow \Gamma_{\psi^+}$ , we can arrive at the analytical expressions for other channels of coannihilation.

### Acknowledgements

RI thanks the SERB-DST, India for the research grant EMR/2015/000333. SC would like to thank MHRD, Government of India for research fellowship. The authors acknowledge useful discussions with Poulouse Poulouse, Sunando Patra and Pratishruti Saha.

- 
- [1] G. Hinshaw *et al.* (WMAP), *Astrophys. J. Suppl.* **208**, 19 (2013), [arXiv:1212.5226 \[astro-ph.CO\]](#).
  - [2] N. Aghanim *et al.* (Planck), (2018), [arXiv:1807.06209 \[astro-ph.CO\]](#).
  - [3] L. Bergström, *Rept. Prog. Phys.* **63**, 793 (2000), [arXiv:hep-ph/0002126 \[hep-ph\]](#).
  - [4] G. Bertone, D. Hooper, and J. Silk, *Phys. Rept.* **405**, 279 (2005), [arXiv:hep-ph/0404175 \[hep-ph\]](#).
  - [5] J. L. Feng, *Ann. Rev. Astron. Astrophys.* **48**, 495 (2010), [arXiv:1003.0904 \[astro-ph.CO\]](#).
  - [6] V. Silveira and A. Zee, *Phys. Lett.* **161B**, 136 (1985).
  - [7] J. McDonald, *Phys. Rev.* **D50**, 3637 (1994), [arXiv:hep-ph/0702143 \[HEP-PH\]](#).
  - [8] C. P. Burgess, M. Pospelov, and T. ter Veldhuis, *Nucl. Phys.* **B619**, 709 (2001), [arXiv:hep-ph/0011335 \[hep-ph\]](#).
  - [9] P. Athron *et al.* (GAMBIT), *Eur. Phys. J. C* **77**, 568 (2017), [arXiv:1705.07931 \[hep-ph\]](#).
  - [10] G. Arcadi, A. Djouadi, and M. Raidal, (2019), [arXiv:1903.03616 \[hep-ph\]](#).
  - [11] P. Agnes *et al.* (DarkSide), *Phys. Rev.* **D93**, 081101 (2016), [Addendum: *Phys. Rev.* **D95**, no.6, 069901 (2017)], [arXiv:1510.00702 \[astro-ph.CO\]](#).
  - [12] D. S. Akerib *et al.* (LUX), *Phys. Rev. Lett.* **118**, 021303 (2017), [arXiv:1608.07648 \[astro-ph.CO\]](#).
  - [13] E. Aprile *et al.* (XENON), *Phys. Rev. Lett.* **119**, 181301 (2017), [arXiv:1705.06655 \[astro-ph.CO\]](#).
  - [14] X. Cui *et al.* (PandaX-II), *Phys. Rev. Lett.* **119**, 181302 (2017), [arXiv:1708.06917 \[astro-ph.CO\]](#).
  - [15] A. Albert *et al.* (Fermi-LAT, DES), *Astrophys. J.* **834**, 110 (2017), [arXiv:1611.03184 \[astro-ph.HE\]](#).

- [16] M. Ackermann *et al.* (Fermi-LAT), *Phys. Rev.* **D91**, 122002 (2015), [arXiv:1506.00013 \[astro-ph.HE\]](#) .
- [17] A. Abramowski *et al.* (H.E.S.S.), *Phys. Rev. Lett.* **110**, 041301 (2013), [arXiv:1301.1173 \[astro-ph.HE\]](#) .
- [18] G. Belanger, B. Dumont, U. Ellwanger, J. F. Gunion, and S. Kraml, *Phys. Rev.* **D88**, 075008 (2013), [arXiv:1306.2941 \[hep-ph\]](#) .
- [19] G. Aad *et al.* (ATLAS), *JHEP* **11**, 206 (2015), [arXiv:1509.00672 \[hep-ex\]](#) .
- [20] V. Khachatryan *et al.* (CMS), *JHEP* **02**, 135 (2017), [arXiv:1610.09218 \[hep-ex\]](#) .
- [21] G. Belanger, K. Kannike, A. Pukhov, and M. Raidal, *JCAP* **1301**, 022 (2013), [arXiv:1211.1014 \[hep-ph\]](#) .
- [22] S. Bhattacharya, A. Drozd, B. Grzadkowski, and J. Wudka, *JHEP* **10**, 158 (2013), [arXiv:1309.2986 \[hep-ph\]](#) .
- [23] L. Bian, R. Ding, and B. Zhu, *Phys. Lett.* **B728**, 105 (2014), [arXiv:1308.3851 \[hep-ph\]](#) .
- [24] B. Batell, N. Lange, D. McKeen, M. Pospelov, and A. Ritz, *Phys. Rev.* **D95**, 075003 (2017), [arXiv:1606.04943 \[hep-ph\]](#) .
- [25] P. Bandyopadhyay, E. J. Chun, and R. Mandal, *Phys. Lett.* **B779**, 201 (2018), [arXiv:1709.08581 \[hep-ph\]](#) .
- [26] L. Wang, X.-F. Han, and B. Zhu, *Phys. Rev.* **D98**, 035024 (2018), [arXiv:1801.08317 \[hep-ph\]](#) .
- [27] K. Griest and D. Seckel, *Phys. Rev.* **D43**, 3191 (1991).
- [28] J. R. Ellis, T. Falk, and K. A. Olive, *Phys. Lett.* **B444**, 367 (1998), [arXiv:hep-ph/9810360 \[hep-ph\]](#) .
- [29] J. Ellis, F. Luo, and K. A. Olive, *JHEP* **09**, 127 (2015), [arXiv:1503.07142 \[hep-ph\]](#) .
- [30] M. J. Baker and A. Thamm, *JHEP* **10**, 187 (2018), [arXiv:1806.07896 \[hep-ph\]](#) .
- [31] M. J. Baker *et al.*, *JHEP* **12**, 120 (2015), [arXiv:1510.03434 \[hep-ph\]](#) .
- [32] S. Biondini and S. Vogl, (2019), [arXiv:1907.05766 \[hep-ph\]](#) .
- [33] A. Ibarra, A. Pierce, N. R. Shah, and S. Vogl, *Proceedings, Meeting of the APS Division of Particles and Fields (DPF 2015): Ann Arbor, Michigan, USA, 4-8 Aug 2015*, *Phys. Rev.* **D91**, 095018 (2015), [arXiv:1501.03164 \[hep-ph\]](#) .
- [34] V. V. Khoze, A. D. Plascencia, and K. Sakurai, *JHEP* **06**, 041 (2017), [arXiv:1702.00750 \[hep-ph\]](#) .
- [35] D. Borah, S. Sadhukhan, and S. Sahoo, *Phys. Lett.* **B771**, 624 (2017), [arXiv:1703.08674 \[hep-ph\]](#) .
- [36] M. Tanabashi *et al.* (Particle Data Group), *Phys. Rev.* **D98**, 030001 (2018).
- [37] R. M. Godbole, M. Guchait, and D. P. Roy, *Phys. Rev.* **D79**, 095015 (2009), [arXiv:0807.2390 \[hep-ph\]](#) .
- [38] T. Jittoh, J. Sato, T. Shimomura, and M. Yamanaka, *Phys. Rev.* **D73**, 055009 (2006), [Erratum: *Phys. Rev.* **D87**, no.1, 019901 (2013)], [arXiv:hep-ph/0512197 \[hep-ph\]](#) .
- [39] S. Kaneko, J. Sato, T. Shimomura, O. Vives, and M. Yamanaka, *Phys. Rev.* **D87**, 039904 (2013), [*Phys. Rev.* **D78**, no.11, 116013 (2008)], [arXiv:0811.0703 \[hep-ph\]](#) .
- [40] T. Jittoh, K. Kohri, M. Koike, J. Sato, T. Shimomura, and M. Yamanaka, *Phys. Rev.* **D82**, 115030 (2010), [arXiv:1001.1217 \[hep-ph\]](#) .
- [41] M. Citron, J. Ellis, F. Luo, J. Marrouche, K. A. Olive, and K. J. de Vries, *Phys. Rev.* **D87**, 036012 (2013), [arXiv:1212.2886 \[hep-ph\]](#) .
- [42] Y. Konishi, S. Ohta, J. Sato, T. Shimomura, K. Sugai, and M. Yamanaka, *Phys. Rev.* **D89**, 075006 (2014), [arXiv:1309.2067 \[hep-ph\]](#) .
- [43] N. Desai, J. Ellis, F. Luo, and J. Marrouche, *Phys. Rev.* **D90**, 055031 (2014), [arXiv:1404.5061 \[hep-ph\]](#) .
- [44] G. B  flanger, F. Boudjema, A. Pukhov, and A. Semenov, *Comput. Phys. Commun.* **192**, 322 (2015), [arXiv:1407.6129 \[hep-ph\]](#) .
- [45] R. Barbieri, L. J. Hall, and V. S. Rychkov, *Phys. Rev.* **D74**, 015007 (2006), [arXiv:hep-ph/0603188 \[hep-ph\]](#) .
- [46] E. Aprile *et al.* (XENON), (2018), [arXiv:1805.12562 \[astro-ph.CO\]](#) .
- [47] A. Alloul, N. D. Christensen, C. Degrande, C. Duhr, and B. Fuks, *Comput. Phys. Commun.* **185**, 2250 (2014), [arXiv:1310.1921 \[hep-ph\]](#) .
- [48] J. Alwall, R. Frederix, S. Frixione, V. Hirschi, F. Maltoni, O. Mattelaer, H. S. Shao, T. Stelzer, P. Torrielli, and M. Zaro, *JHEP* **07**, 079 (2014), [arXiv:1405.0301 \[hep-ph\]](#) .
- [49] T. Sjostrand, S. Ask, J. R. Christiansen, R. Corke, N. Desai, P. Ilten, S. Mrenna, S. Prestel, C. O. Rasmussen, and P. Z. Skands, *Comput. Phys. Commun.* **191**, 159 (2015), [arXiv:1410.3012 \[hep-ph\]](#) .
- [50] J. de Favereau, C. Delaere, P. Demin, A. Giammanco, V. Lema  tre, A. Mertens, and M. Selvaggi (DELPHES 3), *JHEP* **02**, 057 (2014), [arXiv:1307.6346 \[hep-ex\]](#) .
- [51] A. Hocker *et al.*, (2007), [arXiv:physics/0703039 \[physics.data-an\]](#) .
- [52] M. Cacciari, G. P. Salam, and G. Soyez, *Eur. Phys. J.* **C72**, 1896 (2012), [arXiv:1111.6097 \[hep-ph\]](#) .